Journal of Biomechanics 84 (2019) 103–112

Contents lists available at ScienceDirect

Journal of Biomechanics

journal homepage: www.elsevier.com/locate/jbiomech
www.JBiomech.com

Numerical design of a microfluidic chip for probing mechanical properties of cells

Ting Ye [a,*], Huixin Shi [a], Nhan Phan-Thien [b], Chwee Teck Lim [b,c,d], Yu Li [a]

[a] Department of Computational Mathematics, Jilin University, China
[b] Department of Mechanical Engineering, National University of Singapore, Singapore
[c] Department of Biomedical Engineering, National University of Singapore, Singapore
[d] Mechanobiology Institute, National University of Singapore, Singapore

ARTICLE INFO

Article history:
Accepted 12 December 2018

Keywords:
Smoothed dissipative particle dynamics
Immersed boundary method
Mechanical properties
Microfluidic chip
Red blood cell
Malaria

ABSTRACT

Microfluidic chips have been widely used to probe the mechanical properties of cells, which are recognized as a promising label-free biomarker for some diseases. In our previous work (Ye et al., 2018), we have studied the relationships between the transit time and the mechanical properties of a cell flowing through a microchannel with a single constriction, which potentially forms a basis for a microfluidic chip to measure cell's mechanical properties. Here, we investigate this microfluidic chip design and examine its potential in performances. We first develop the simultaneous dependence of the transit time on both the shear and bending moduli of a cell, and then examine the chip sensitivity with respect to the cell mechanical properties while serializing a single constriction along the flow direction. After that, we study the effect of the flow velocity on the transit time, and also test the chip's ability to identify heterogeneous cells with different mechanical properties. The results show that the microfluidic chip designed is capable of identifying heterogeneous cells, even when only one unhealthy cell is included. The serialization of chip can greatly increase the chip sensitivity with respect to the mechanical properties of cells. The flow with a higher velocity helps in not only promoting the chip throughput, but also in providing more accurate transit time measurements, because the cell prefers a symmetric deformation under a high velocity.
© 2018 Elsevier Ltd. All rights reserved.

1. Introduction

Some diseases not cause only biological and functional alterations, but also abnormalities in the structural and mechanical properties of cells, for examples, in cancer, malaria, and sickle cell anemia (Suresh et al., 2005; Hosseini and Feng, 2012). It has been shown that cancer cells may constantly change their stiffness as they progress to their malignant state while undergoing metastasis, and generally, they have lower stiffness but higher motility than their benign or healthy counterparts (Suresh, 2006; Darling et al., 2007). The mechanical changes in cells have been recognized as a promising new biomarker of diseases, in addition to the conventional diagnostic techniques based on biological and functional alterations (Xu et al., 2012; Nematbakhsh and Lim, 2015; Suresh et al., 2015; Pivkin et al., 2016). Hence, it is important and necessary to measure mechanical properties of cells for a better understanding of the pathophysiology and pathogenesis of a variety of human diseases.

Microfluidic devices have attracted increasing interests in measuring mechanical properties of cells due to their special advantages, and also because microfluidic technologies have made significant improvements in recent years (Whitesides, 2006; Huang et al., 2012). They can be made higher throughput, have the ability to identify cell heterogeneity, as well as being inexpensive and simple to operate. One of widely-used designs is by placing various constrictions along the microchannels, the necessary pressure or the transit time of cells squeezed through these constrictions can be measured; and from these the cell's mechanical properties can be deduced. Shelby et al. (2003) were among the firsts to use a microfluidic chip with a single square constriction to study whether infected red blood cells (RBCs) can block capillaries that have diameters smaller than that of the infected RBC. Hou et al. (2009) used a similar microfluidic device to probe the deformability of breast cancer cells, and to distinguish non-malignant and malignant cells, based on the differences in stiffness between them which can be inferred from their transit times and velocities. However, this single-constriction design not only limits the overall throughput, but also decreases the measuring sensitivity. To address these issues, Bow et al. (2011) proposed

* Corresponding author.
E-mail address: yeting@jlu.edu.cn (T. Ye).

https://doi.org/10.1016/j.jbiomech.2018.12.019
0021-9290/© 2018 Elsevier Ltd. All rights reserved.

an automated microfabricated "deformability cytometer" with many triangle-shaped pillars periodically spaced along the flow direction (or "serialization") and its perpendicular direction (or "parallelization"). They suggested that their device is especially applicable to characterize the mechanical properties of heterogeneous cells in a high-throughput manner. Similar designs were then adopted and extended in later studies. Guo et al. (2012, 2014) developed a serialized microfluidic device with multiple funnel-shaped constrictions, and can clearly differentiate malaria-infected RBCs from healthy RBCs with precisely controlled pressure. Gambhire et al. (2017) adopted a parallelized microfluidic device with high aspect ratio slits to study the deformation of healthy and sickle RBCs.

Along with the experiments, numerical simulations have also been carried out to investigate the motion and deformation of cells through such microfluidic chips with constrictions. These studies mainly focused on a single-constriction microchannel, with periodic boundary conditions considered. For example, Xiao et al. (2014) simulated a single RBC through a stenosis microvessel using dissipative particle dynamics (DPD), and two RBCs as well (Xiao et al., 2016). Moon et al. (2016) carried out a similar simulation on a single RBC by lattice Boltzmann method (LBM). Ye et al. (2018b) used a smoothed dissipative particle dynamics (SDPD) to study the relationship between the transit time and mechanical properties of a single cell through a constricted microchannel. Serrano-Alcalde et al. (2017) and Casquero et al. (2017) simulated a circulating tumor cell (CTC) through the constricted microchannel by a commercial software (ABAQUS) and immersed boundary method (IBM), respectively, where the CTC is modeled as a compound capsule with a nucleus (different to a RBC). Furthermore, some numerical studies were done on multiple RBCs through a constricted microchannel. Polwaththe-Gallage et al. (2016a,b) used a coupled smoothed particle hydrodynamics - discrete element method (SPH-DEM) approach to investigate the deformation of five RBCs through a stenosed capillary; Koohyar et al. (2016) used a finite volume method (FVM) for a case with a large number RBCs.

Our current work started from the "deformability cytometer" designed by Bow et al. (2011), and continued to explore our previous study on the relationship between the transit time and mechanical properties of a cell in a stenosed microchannel (Ye et al., 2018b), and examined the designed microfluidic chip in its ability to identify heterogeneous cells.

2. Models and methods

The microfluidic chip is schematically depicted in Fig. 1. It is constructed by periodically extending a unit element (Fig. 1b) along the flow direction (*i.e.*, serialization) and its perpendicular direction (*i.e.*, parallelization). The serialization helps to increase the sensitivity of the measurement, while the parallelization helps to increase the cell throughput. In the simulation, the unit element is considered as the flow domain, with $L = 100$ μm, $W = 10$ μm and $H = 10$ μm, employing the full periodicity boundary conditions. Its constriction is built by embedding two right trapezoidal pillars, with $d_1 = 1$ μm, $d_2 = 3$ μm and $L_s = 10$ μm. These dimensions have been verified as a preferable choice for measuring the mechanical properties of a cell (Ye et al., 2018b).

To develop the numerical model, we here use smoothed dissipative particle dynamics (SDPD), a particle-based method (Litvinov et al., 2009, 2010; Bian et al., 2012). Its theory is well established, and we only outline the general formulation for completeness. SDPD is derived from Navier-Stokes (NS) equations, which govern the motion of fluids interior and exterior to the cell (Peskin, 2002; Tian et al., 2018),

$$\nabla \cdot \boldsymbol{v} = 0, \tag{1}$$

$$\rho \frac{d\boldsymbol{v}}{dt} = -\nabla P + \eta \nabla^2 \boldsymbol{v} + \rho \boldsymbol{g} + \boldsymbol{f}, \tag{2}$$

$$\boldsymbol{f}(\boldsymbol{x}, t) = \int_\Gamma \left[\boldsymbol{f}^{def}(r, s, t) + \boldsymbol{f}^{agg}(r, s, t)\right] \delta(\boldsymbol{x} - \boldsymbol{X}(r, s, t)) dr ds, \tag{3}$$

$$\frac{d\boldsymbol{X}}{dt} = \int_\Omega \boldsymbol{v}(\boldsymbol{x}, t) \delta(\boldsymbol{x} - \boldsymbol{X}(r, s, t)) d\boldsymbol{x}, \tag{4}$$

where the cell membrane is treated as a surface immersed into the fluids. Here $\boldsymbol{v}$, ρ and P are the velocity, density and pressure fields, respectively; t is the time; η is the shear viscosity; $\boldsymbol{g}$ is the externally-applied acceleration to drive the fluid flow; $\boldsymbol{f}$ is the singular force acting on the fluid from the cell membrane; $\boldsymbol{f}_{def}$ and $\boldsymbol{f}_{agg}$ are the force densities acting on the cell membrane due to its deformation and aggregation; $\boldsymbol{X}$ is the position of the cell membrane in the Lagrangian system; $\boldsymbol{x}$ is the position of the fluid in the Eulerian system; (r, s) is a curvilinear coordinate on the cell membrane to label a Lagrangian point; Ω is the computational domain, and Γ refers to the surface domain occupied by the cell membrane. Eq. (4) describes the evolution of the cell membrane.

In the SDPD framework, the computational domain is represented by a set of discrete particles, and each of them associates with physical properties, such as mass, velocity, density, etc. These properties and their derivatives can be approximately interpolated by a kernel function with a compact support, having the form (Español and Revenga, 2003),

$$h(\boldsymbol{x}_i) = \sum_j \frac{K_{ij}}{d_j} h(\boldsymbol{x}_j), \tag{5}$$

$$\nabla h(\boldsymbol{x}_i) = \sum_j \frac{\nabla K_{ij}}{d_j} h(\boldsymbol{x}_j), \tag{6}$$

where $\boldsymbol{x}_i$ is the position of particle i; $h(\boldsymbol{x}_i)$ stands for an arbitrary physical property of the particle i; $d_j = m/\rho_j; m$ is the particle mass (all particles are assumed to have the same mass); ρ_j is the density of particle j; K_{ij} is the kernel function. Substituting Eqs. (5) and (6) into Eqs. (1)–(4), the NS equations are then converted into a discrete form as (Español and Revenga, 2003; Pivkin et al., 2011; Imai et al., 2016; Gompper and Fedosov, 2016; Ye et al., 2016),

$$d\boldsymbol{x}_i = \boldsymbol{v}_i dt, \tag{7}$$

$$m d\boldsymbol{v}_i = \boldsymbol{F}_C dt + \boldsymbol{F}_D dt + \boldsymbol{F}_R + \boldsymbol{F}_G dt + \boldsymbol{F}_B dt, \tag{8}$$

$$\boldsymbol{F}_B = \sum_k \frac{K_{ik}}{d_i} \left(\boldsymbol{F}_k^{def} + \boldsymbol{F}_k^{agg}\right), \tag{9}$$

$$\frac{d\boldsymbol{X}_k}{dt} = \sum_i \frac{K_{ik}}{d_i} \boldsymbol{v}_i, \tag{10}$$

where $\boldsymbol{v}_i$ is the velocity of the fluid particle i, and $\boldsymbol{X}_k$ is the position of the membrane particle k. The forces $\boldsymbol{F}_C$, $\boldsymbol{F}_D$ correspond to the terms $-\nabla P$ and $\eta \nabla^2 \boldsymbol{v}$ in Eq. (2), called conservative and dissipative forces, respectively. They are related to the fluid compressibility and viscosity. The force $\boldsymbol{F}_R$ is added to describe the random fluctuations of particles, to maintain a constant Boltzmann temperature (specific kinetic energy) of the fluid. The force $\boldsymbol{F}_G$ corresponds to $\rho \boldsymbol{g}$ in Eq. (2), the externally-applied force to drive the flow. Eqs. (9) and (10) reflect the main idea of the immersed boundary method (IBM) (Peskin, 2002), taking account of the cell-fluid interactions. The deformation force $\boldsymbol{F}_k^{def}$ and the aggregation force $\boldsymbol{F}_k^{agg}$ acting on the cell membrane are converted by Eq. (9) to the force $\boldsymbol{F}_B$, which is a singular force acting on the fluid around the cell membrane, reflecting the action of the cell on the fluid. The position $\boldsymbol{X}_k$ of the cell membrane is updated with the fluid velocity $\boldsymbol{v}_i$ by

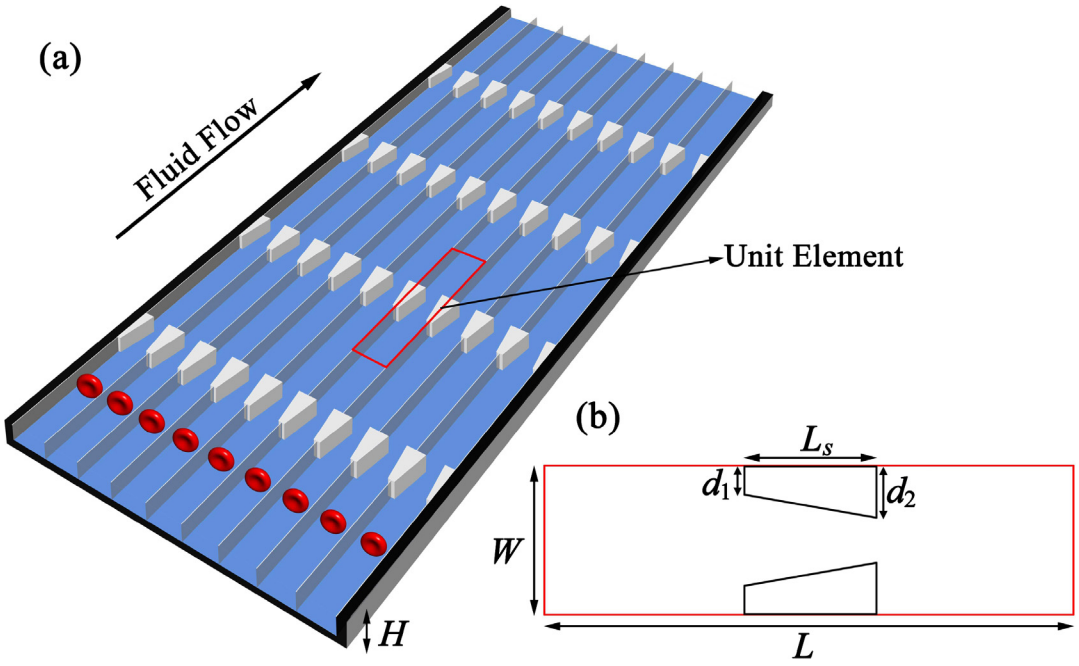

Fig. 1. (a) Schematic diagram of a microfluidic chip for measuring mechanical properties of cells, by constructing a periodic array of a unit element along the flow (serialization) and its perpendicular direction (parallelization). (b) The simulation domain, the unit element with periodicity boundary conditions.

Eq. (10), reflecting the action of the fluid on the cell. More detailed information can be found in our previous work (Ye et al., 2017b,c, 2018a).

Now we turn our attention to the RBC model, *i.e.*, formulating $\boldsymbol{F}_k^{def}$ and $\boldsymbol{F}_k^{agg}$ in Eq. (9). The cell membrane is modeled as a triangular network via connecting the discrete membrane particles. This network is endowed with a potential deformation energy U_{def}, consisting of the four types of energies: (i) the in-plane energy U_s to describe the membrane shear deformation, (ii) the bending energy U_b to describe the membrane bending deformation, (iii) the area-restraint energy U_a to conserve the membrane surface area, and (iv) the volume-restraint energy U_v to conserve the cell volume (Skalak et al., 1973; Li et al., 2005; Pivkin and Karniadakis, 2008; Hosseini and Feng, 2009; Fedosov et al., 2010b; Moon et al., 2016),

$$U_{def} = U_s + U_b + U_a + U_v, \tag{11}$$

and thus the deformation force can be expressed by

$$\boldsymbol{F}_k^{def} = -\frac{\partial U_{def}}{\partial \boldsymbol{X}_k}. \tag{12}$$

The detailed expressions about the four types of energies can be found in the work of Fedosov et al. (2010a, 2011, 2014) The cell mechanical properties determined by this cell model, including the shear modulus E_S, bending modulus E_B and dilation modulus E_D, are approximated as (Fedosov et al., 2010a),

$$E_S = \frac{\sqrt{3}k_BT}{4p_jl_j^0}\left[\frac{s_0}{2(1-s_0)^3} + \frac{1}{2(1-s_0)^2} + 3s_0 - \frac{1}{2}\right], \tag{13}$$

$$E_B = \frac{2}{\sqrt{3}}K_B, \tag{14}$$

$$E_D = 2E_S + K_{AG} + K_{AL}, \tag{15}$$

where k_BT, p_j, l_j^0, s_0, K_B, K_{AG} and K_{AL} are Boltzmann temperature, persistence length, reference length of triangular edge, relative length of triangular edge, bending coefficient, global area coefficient and local area coefficient, respectively.

The aggregation force $\boldsymbol{F}_k^{agg}$ in Eq. (9) is present only when multiple cells are considered. Currently, there are two main theoretical model to describe the cell-cell interaction, the bridging model (Chien and Jan, 1973; Bagchi et al., 2005) and the depletion model (Skalak et al., 1981; Neu and Meiselman, 2002). The former assumes that the cell aggregation is attributed to the bridging of macromolecules between the cells, such as fibrinogen or dextran, while the latter proposes that the cell aggregation results from the existence of the polymer depletion layer between the cells. Mathematically, these two models are so complex that they are not widely used in numerical simulations (Chung et al., 2007). To simplify the depletion model, Liu and Liu (2006) proposed a Morse potential function to fit the total interaction energy, which has been accepted in various simulations of multiple cells (Zhang et al., 2008, 2009; Ye et al., 2014). In our present work, we also adopt this simplified model, where the interaction energy between two facing unit flat planes is expressed as a Morse potential (Liu and Liu, 2006),

$$\phi(r) = E_I\left[e^{2\beta(r_0-r)} - 2e^{\beta(r_0-r)}\right], \tag{16}$$

where E_I is the surface energy; β is a scaling factor; r_0 is the zero force separation; r is the local distance between two facing unit flat planes. The total interaction energy U^{agg} of the cell membrane, *i.e.*, the triangular network, is thus given by (Ye et al., 2014),

$$U^{agg} = \sum_{m=1,\cdots,N_t} \phi(r_{mm'})(\boldsymbol{n}_m \cdot \boldsymbol{k}_m)(\boldsymbol{n}_{m'} \cdot \boldsymbol{k}_{m'})A_m, \tag{17}$$

where the subscripts m and m' refer to the triangles m and m' of the two respective cells; $\boldsymbol{n}$ is the outward unit normal vector of the triangle; $\boldsymbol{k}$ is the unit vector in the direction parallel to the line joining the centers of two interacting cells; A_m is the area of the triangle m, and N_t is the number of triangles. Note that the terms $\boldsymbol{n}_m \cdot \boldsymbol{k}_m$ and $\boldsymbol{n}_{m'} \cdot \boldsymbol{k}_{m'}$ are introduced to consider two curved surfaces instead of flat planes (Bhattacharjee et al., 1998; Chung et al., 2007). Hence, the aggregation force is expressed as

$$\boldsymbol{F}_k^{agg} = -\frac{\partial U^{agg}}{\partial \boldsymbol{X}_k}. \tag{18}$$

The velocity-Verlet algorithm (Groot and Warren, 1997; Ye et al., 2017a) is used to numerically solve Eqs. (7) and (8), because of its high computational efficiency. Its procedure is briefly listed as: (i) updating the positions of each fluid particle and each membrane particle, (ii) predicting the fluid velocity, (iii) calculating all the forces; (iv) correcting the velocity by the updated forces.

3. Results and discussions

3.1. Validation

Two validation studies were offered here to establish the reliability of our models. One was for a single RBC, and the other was for multiple RBCs.

In the first validation, a RBC was squeezed through a narrow microchannel with a square cross section of $4 \times 4\ \mu m^2$ and a length of 40 μm, under a pressure differential of 1.5 mm of water. Both ends of the narrow microchannel were connected to two wider trapezoidal nozzles, and the whole channel was 72, 4 and 32 μm in length, width and height, respectively. The RBC mechanical properties were given as: shear modulus $E_S = 6.0 \times 10^{-6}$ N/m, bending modulus $E_B = 2.4 \times 10^{-19}$ J, dilation modulus $E_D = 6 \times 10^{-4}$ N/m. The fluid physical properties were given as: density $\rho = 10^3$ kg/m^3, viscosity $\eta = 10^{-4}$ Pa·s, external acceleration $\boldsymbol{g}$ = (245, 0, 0) m/s^2. This external acceleration generated the average velocity to be about v_m = 1.22 mm/s in the narrow microchannel. Several dimensionless groups related to this validation: capillary number $Ca = \eta v_m / E_S$ = 0.02, dimensionless bending modulus $\overline{E}_B = E_B / \left(E_S R_e^2\right) = 5 \times 10^{-3}$, and dimensionless dilation modulus $\overline{E}_D = E_D / E_S = 100$, where R_e is effective radius defined as $R_e = \sqrt[3]{3V/(4\pi)}$ and V is the cell volume. These values were similar to those in the experiments of Li et al. (2007) and in the previous simulations of Xiao et al. (2014) Fig. 2 shows a comparison of the RBC deformation. The RBC experienced severe deformation in passing through the microchannel. When the RBC was about to enter the constriction, the main cell body seemed to be absorbed into the narrow microchannel. After the whole RBC was squeezed into the narrow microchannel, it folded itself to fit the microchannel width and was elongated along the flow direction. It recovered quickly its biconcave shape once exited from the constriction. The deformation pattern was in good agreements with experiments (Li et al., 2007) and with previous simulations (Xiao et al., 2014).

In the second validation, five RBCs were considered to flow through a stenosed cylindrical microchannel, with a length of 57.2 μm and a diameter of 10 μm. The stenosis was formed by two round corners with a radius of 3.2 μm, and had a minimum diameter of 6.8 μm. The RBC closest to the stenosed section was labeled as the 1st RBC (the leading RBC), the RBC closest the inlet as the 5th RBC (the trailing RBC), and the other RBCs were numbered in consecutive order. The intercellular distance was set to 4 μm. Their mechanical properties were set as: shear modulus $E_S = 4.5 \times 10^{-7}$ N/m, bending modulus $E_B = 4 \times 10^{-18}$ J and dilation modulus $E_D = 5 \times 10^{-3}$ N/m. The fluid physical properties were set as: density $\rho = 10^3$ kg/m^3 and viscosity $\eta = 10^{-3}$ Pa·s. All of these parameters were the same as those used by Polwaththe-Gallage et al. (2016a) Nevertheless, there were still three differences between our conditions and theirs. One was that the flow was driven by a pressure difference of 1000 Pa in their work, while it was by the external acceleration in our work and it was set as $\boldsymbol{g} = \left(1.75 \times 10^4, 0, 0\right)$ m/s^2. These two driven ways can generate the same velocity field for a tube flow. The other difference was that the cytoplasm viscosity was assumed to be same as that of suspending fluid in our work, but in their work, the cytoplasm viscosity was 5 times greater. The last difference was that we considered a weak intercellular interaction with a strength of $E_I = 10^{-7}$ N/m, but this interaction was completely neglected in their work. Fig. 3 shows a comparison of deformed shapes of the RBCs between our and their work, where the similar deformations were observed at each time instant. All RBCs were travelled with the fluid, and squeezed through the stenosed section. The 1st RBC showed more deformation compared with subsequent RBCs. A difference was that our RBCs arrived to the same position of the microchannel earlier than theirs. For example, the 1st RBC in our work arrived to the stenosed section at t = 0.14 ms, but at t = 0.2 ms in their work, as shown in Fig. 3(c) and (i). The cytoplasm was assumed to be the same fluid as the suspending fluid in our work, but 5 times more viscous in their work (Polwaththe-Gallage et al., 2016a). Hence, the fluid in our work flowed faster, which carried the RBCs to the same position of the stenosed microchannel sooner. Fig. 4 shows the variation of the deformation index DI and the mean velocity v_c of the five RBCs with time. As expected, each RBC experienced the largest deformation when flowing through the stenosed section, with DI = 1.359, 1.273, 1.295, 1.234 and 1.267, respectively, compared with 1.444, 1.321, 1.332, 1.343 and 1.356 in the work of Polwaththe-Gallage et al. (2016a) Moreover, all RBCs flowed at almost a similar mean velocity about v_c = 0.13 m/s through the stenosed section, close to the value of about 0.135 m/s reported in the work of Polwaththe-Gallage et al. (2016a).

3.2. Cell mechanical properties

In our previous work (Ye et al., 2018b), we proposed two expressions to evaluate the cell mechanical properties. One was the relationship between the transit time and shear modulus of a cell through the microfluidic chip, under the fixed cell bending modulus; the other was the relationship between the transit time and bending modulus, but under the fixed shear modulus of the cell. Both the relationships were obtained from a single-factor analysis. In this section, we provided a general expression of the transit time with respect to both the shear and bending moduli of the cell together. This was a two-factor analysis. We considered a range of the shear modulus $E_S \in [0.1, 300]$ μN/m and the bending modulus $E_B \in [2.0, 120] \times 10^{-19}$ J. This range covered most of biological cells. The flow properties were set as: density $\rho = 10^3$ kg/m^3, viscosity $\eta = 10^{-4}$ Pa·s, external acceleration $\boldsymbol{g}$ = (271.6, 0, 0) m/s^2. This external acceleration generated the average velocity about v_m = 0.01 m/s for the fluid flow in the unconstricted part of the microchannel in the absence of the cell.

Fig. 5 shows the transit time T and its fitting surface, with respect to the shear modulus E_S and the bending modulus E_B, where T was scaled by $l'(m'\varepsilon')^{1/2}$, E_S was scaled by ε'/l'^2 and E_B was scaled by ε'. For convenience, the scaled parameters were denoted as $\hat{T}, \hat{E}_S$ and $\hat{E}_B$, respectively. Note that l', m' and ε' were the cut-off radius, the mass of each SDPD particle and the Boltzmann temperature of the system. They were chosen as the characteristic length, mass and energy, respectively, and set to be l' = 1 μm, $m' = 1.25 \times 10^{-16}$ kg and $\varepsilon' = 4.142 \times 10^{-21}$ J. The fitting surface was generated by the '1stOpt' software developed by 7D-Soft High Technology (Zhang et al., 2013), expressed as

$$\hat{T} = \frac{c_1 + c_2 \ln \hat{E}_S + c_3 \ln \hat{E}_S^2 + c_4 \ln \hat{E}_B + c_5 \ln \hat{E}_B^2 + c_6 \ln \hat{E}_B^3}{1 + c_7 \ln \hat{E}_S + c_8 \ln \hat{E}_S^2 + c_9 \ln \hat{E}_B + c_{10} \ln \hat{E}_B^2}, \tag{19}$$

where c_1 to c_{10} were 10 coefficients with the values of 13.758, −0.587, 0.05, −4.186, 0.262, 0.024, −0.032, 0.003, −0.359 and 0.037. It is essentially a logarithmic rational expression. A conclu-

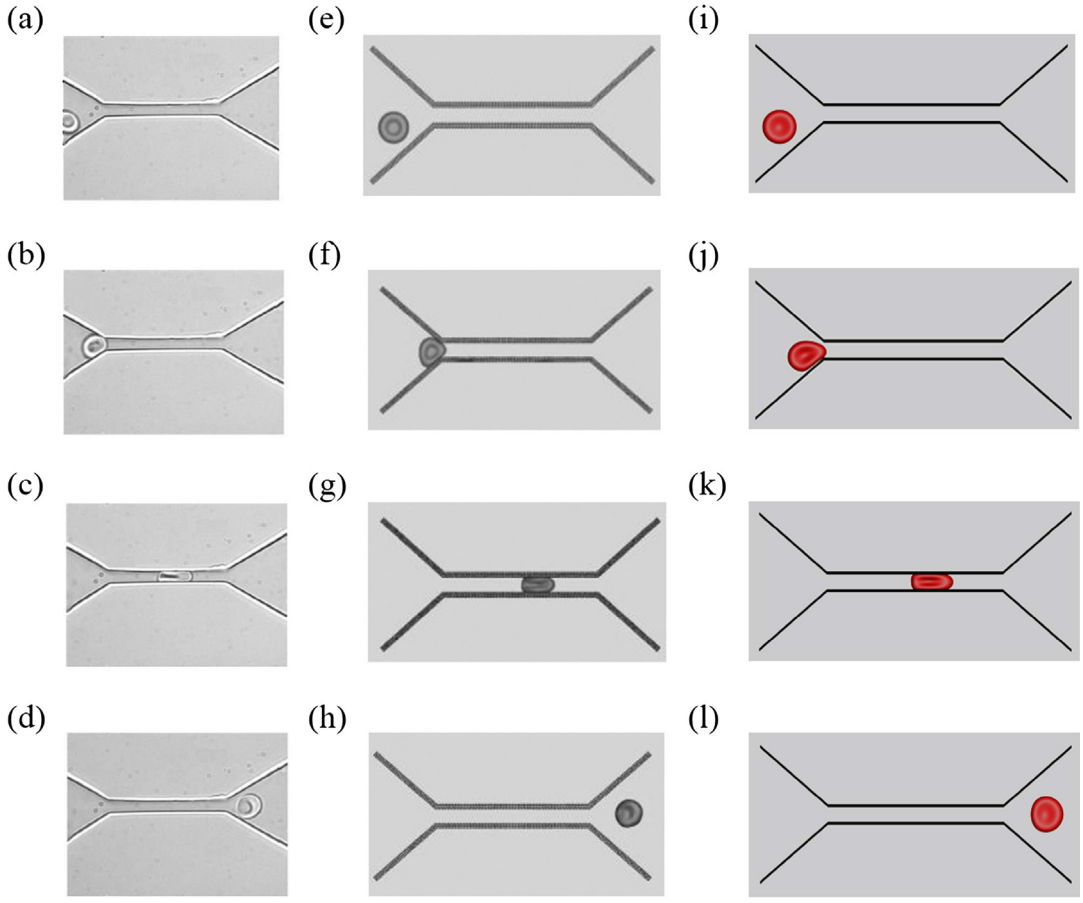

Fig. 2. A comparison of the deformation of a RBC transiting through a narrow microchannel: experimental observations (Li et al., 2007) (a–d), previous numerical simulations (Xiao et al., 2014) (c–h) and our present results (i–l), where the RBC shapes in each row are taken at a similar position in the microchannel.

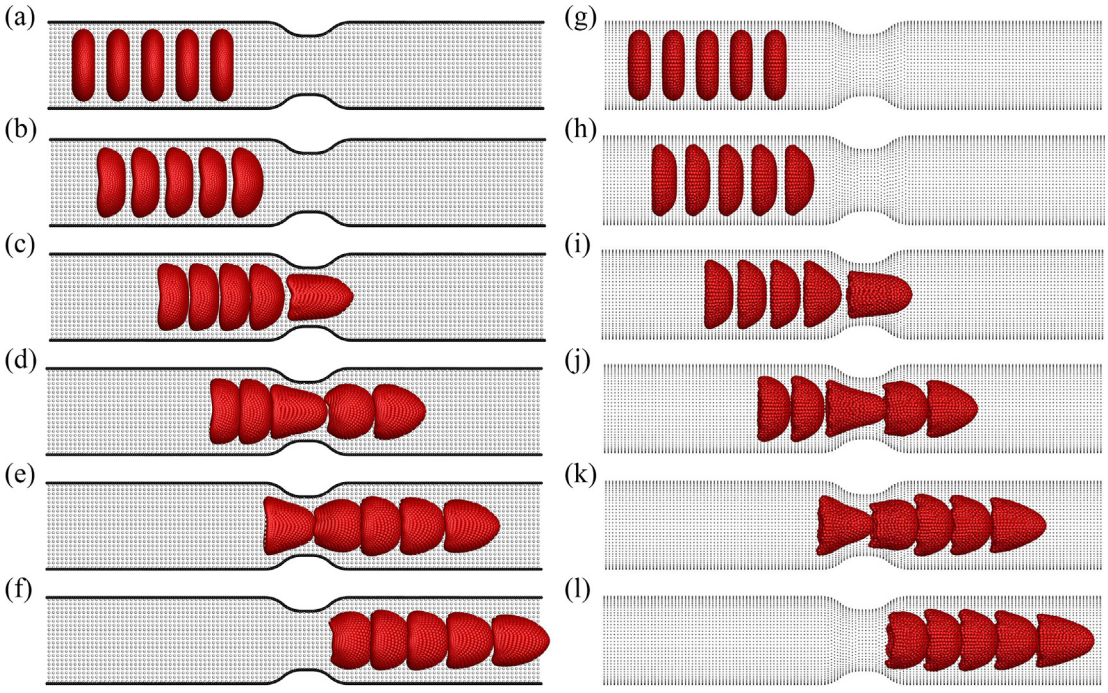

Fig. 3. A comparison of the deformed shapes of five RBCs flowing through a stenosed microchannel: our results (a–f) at t = 0, 0.04, 0.14, 0.24, 0.34 and 0.41 ms, and those obtained by Polwaththe-Gallage et al. (2016a) (g–l) at t = 0, 0.1, 0.2, 0.3, 0.4 and 0.47 ms, respectively.

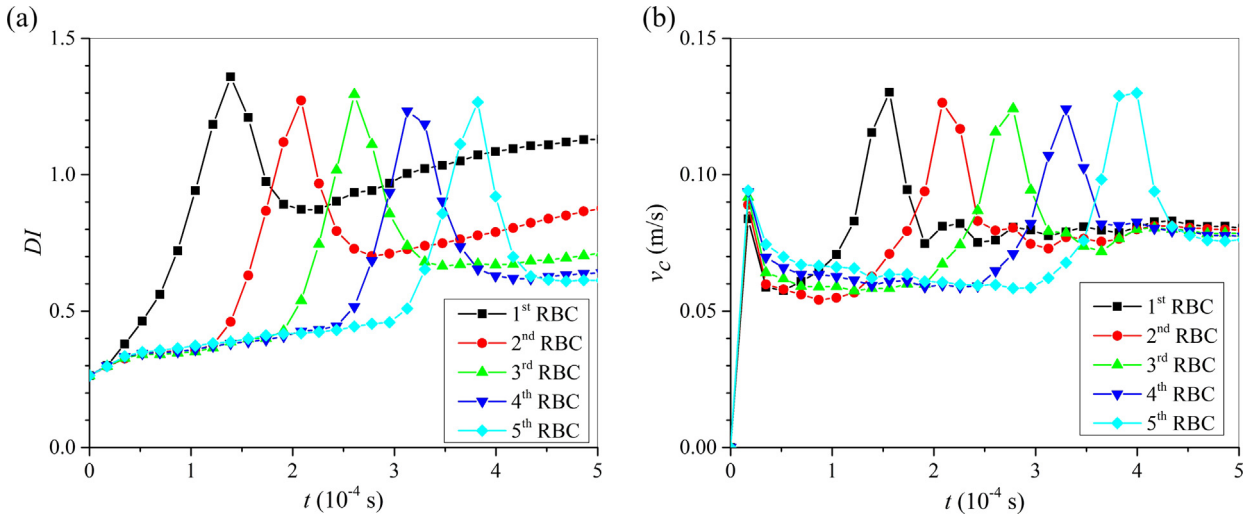

Fig. 4. Evolutions of (a) deformation index (*DI*) and (b) mean velocity (v_c) of five RBCs with time *t*, where *DI* is defined as the ratio of the length of RBC along the flow direction to its width.

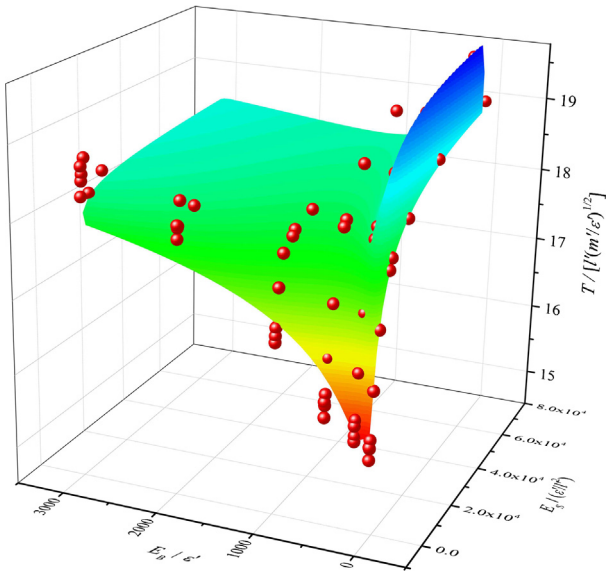

Fig. 5. Fitting of the transit time *T* to the shear modulus E_S and the bending modulus E_B, where the dots are the numerical results, and the surface is the fitting result.

sion is drawn from Eq. (19) that it is impossible to obtain the shear and bending moduli simultaneously, from only one given transit time. However, if one of parameters ($\hat{E}_B$ or $\hat{E}_S$) is known, we can obtain the expression of the transit time with respect to the other parameter, $\hat{T} = f\left(\hat{E}_S\right)$ or $\hat{T} = f\left(\hat{E}_B\right)$. For example, fixing $\hat{E}_B = 50$ yields

$$\hat{T} = \frac{2.829 - 0.597 \ln \hat{E}_S + 0.05 \ln \hat{E}_S^2}{0.163 - 0.032 \ln \hat{E}_S + 0.003 \ln \hat{E}_S^2}, \tag{20}$$

and fixing $\hat{E}_S = 1448$ does

$$\hat{T} = \frac{12.061 - 4.186 \ln \hat{E}_B + 0.262 \ln \hat{E}_B^2 + 0.024 \ln \hat{E}_B^3}{0.926 - 0.359 \ln \hat{E}_B + 0.037 \ln \hat{E}_B^2}. \tag{21}$$

These results were somewhat different with the results obtained by the single-factor analysis in our previous work (Ye et al., 2018b), as shown in Fig. S1 in the Supplementary Material. Especially for the relationship between $\hat{T}$ and $\hat{E}_B$, there was a fluctuation near $\hat{E}_B = 250$ for the transit time obtained by the two-factor analysis. This fluctuation became more obvious as the shear modulus increased further, as shown in Fig. 5. To explain this in details, we took the fixed shear modulus $\hat{E}_S = 72400$ for example, because the fluctuation was very obvious at this value. The transit time increased as $\hat{E}_B$ increased from 50 to 200, but decreased as $\hat{E}_B$ further increased to 3000, such that a fluctuation was formed. As we know, the cell lost the deformability as the bending modulus increased. We observed in our simulations that the cell was folded through the constriction at $\hat{E}_B < 200$, but tilted through the constriction at $\hat{E}_B > 500$. These observations can be seen in the Supplementary Material, which provided the detailed motion and deformation of the cell with the different shear and bending moduli through the constriction. Hence, at $\hat{E}_B < 200$, the cell became more and more difficult to be folded with increasing $\hat{E}_B$, resulting in an increase in the transit time. As $\hat{E}_B$ further increased from 500, however, it tilted more and more, leading to a decrease of the transit time. The fluctuation was mainly attributed to the cell deformability, which, in turn, influenced the motion of the cell through a constriction by either a folded or a tilted shape. Since the shear modulus also affects on the cell deformability, this fluctuation should depend on the cell's shear modulus as well. It was noted that the fluctuation became less and less obvious as the shear modulus decreased, and there was no fluctuation formed at $\hat{E}_S = 24$, as shown in Fig. 5.

3.3. Chip serialization

In our previous work (Ye et al., 2018b), we suggested that a chip serialization can help in increasing the sensitivity of transit time to the variation of mechanical properties. In this section, we implemented the chip serialization and studied the sensitivity of transit time. For this purpose, the unit element in Fig. 1(b) was lengthened to three times, and the fluid properties were same as those in the previous section. The cell properties were set as: $E_S = 6.0 \times 10^{-6}$ N/m, $E_B = 2.4 \times 10^{-19}$ J, $E_D = 6 \times 10^{-4}$ N/m. Thus, the dimensionless groups were: $Ca = 0.1667$, $\overline{E}_B = 0.003$ and $\overline{E}_D = 100$.

Fig. 6 shows the motion and deformation of the cell in this serialized chip. The cell deformed into a square parachute shape from a biconcave shape, before entering the first constriction, and then

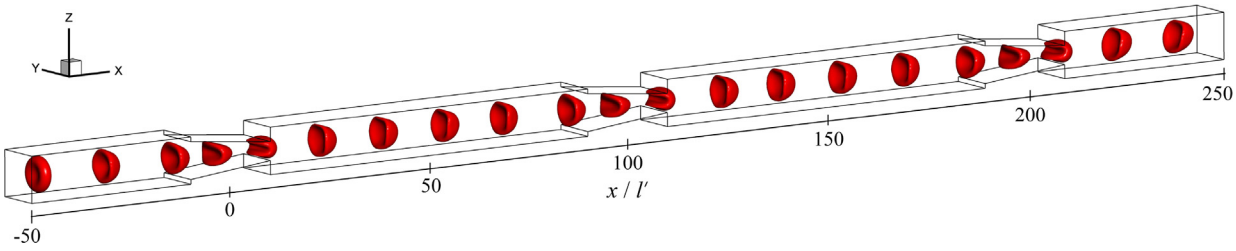

Fig. 6. Motion and deformation of a cell in the serialized chip with three unit elements, where the snapshots from left to right are taken from $t = 0$ to 28.31 ms with the interval of about 1.416 ms, and the the ruler below the figure indicates the microchannel position.

was folded to pass through that constriction. After passing through the first constriction completely, the cell quickly recovered the square parachute shape, ready to pass through the second constriction. A similar deformation occurred for the rest constrictions. Fig. 7 shows a quantitative analysis of the cell deformation, which was measured by the asphericity, defined as (Noguchi and Gompper, 2005),

$$\tau = \frac{1}{2}\frac{\left[(I_1 - I_2)^2 + (I_2 - I_3)^2 + (I_3 - I_1)^2\right]}{(I_1 + I_2 + I_3)^2}, \tag{22}$$

where I_1, I_2 and I_3 were the principal moment of inertia of the equivalent ellipsoid. A general rule is that the rounder the cell, the smaller its asphericity, and it is zero if the cell is deformed into a spherical shape. The asphericity τ in Fig. 7 decreased first, because the cell deformed from the biconcave to the square parachute, becoming somewhat rounder. Then, three peaks appeared, and each of them corresponded to the cell passing through a constriction. When the cell approached to the constriction, the asphericity was relatively small due to the cell having a square parachute shape. As the cell was squeezed into the constriction, it was folded and elongated severely so that its asphericity started to increase. Once the cell left from the constriction, it quickly recovered the square parachute shape and thus the asphericity decreased quickly. Hence, a peak was formed. These three peaks were found to have almost the same profiles, meaning that the cell experienced a similar deformation when passing through the three constrictions. This caused the cell to have a similar transit time, $\hat{T} = 16.365$, 16.654 and 16.671, respectively. An increasing trend was noted, although its increment was very small. Moreover, the cell was slightly tilted after it exited from the third constriction. This tilted RBC did not have enough time to recover its non-tilted shape before crossing from the third constriction to the fourth one, as shown in Fig. S2 in the Supplementary Material, where the serialized chip with five unit elements was considered for examining further the behaviors of exiting cell from the third constriction. The cell assumed a more favorable shape through the fourth constriction, leading to the decrease of the transit time to 16.147. Until the cell exited from the fifth constriction with $\hat{T} = 15.694$, its shape was almost recovered to a non-tilted shape. The decrease of the transit time, caused by the cell having not enough time to recover its original shape, was also observed in the work of Shirai et al. (2003) and Bow et al. (2011). It might be suggested that the cell possibly assumed a periodic cycle on its deformation between a non-tilted and a tilted shape, when it passed through successive constrictions. This might cause the other periodic cycle of the cell transit time with an increasing first and then a decreasing trend. The average transit time of a cell through successive constrictions can thus serve as an indicator of mechanical properties of cell. If the average transit time has a difference of 0.1 ms for two cells with the different mechanical properties through a unit element, the difference will be enlarged to about 10 ms if 100 unit elements are serialized. Hence, the chip serialization can significantly increase the sensitivity of the cell transit time with respect to its mechanical properties.

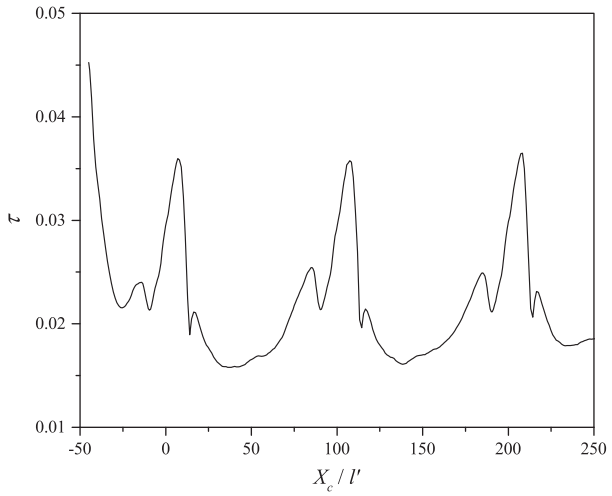

Fig. 7. Asphericity τ of the cell through three constrictions, where X_c refers to the cell centroid and scaled by l'.

3.4. Flow velocity

Past studies have demonstrated that the flow velocity is a key determinant of the cell transit time through a constriction; this has not been covered in our previous work (Ye et al., 2018b). In this section, we examined the effect of the flow velocity. The cell and fluid properties were same as those in the previous section. However, the external acceleration $\boldsymbol{g}$ was set as three different values: (54.32, 0, 0), (271.6, 0, 0) and (679, 0, 0) m/s^2, which generated the mean velocities v_m of about 0.002, 0.01 and 0.05 m/s, respectively, in the unconstricted part of the microchannel. Thus, the dimensionless groups were: $Ca = 0.033$, 0.167 and 0.833 for these three cases, respectively; $\hat{E}_B = 0.003$ and $\hat{E}_D = 100$ in all three cases.

Fig. 8(a)–(c) shows the motion and deformation of the cell subjected to the different velocities of flow. As expected, the larger the flow velocity, the stronger the impact of flow was on the cell, and the more pronounced the cell deformation. Especially, the cell became more and more rounder with increasing the flow velocity, causing the asphericity to decrease, as shown in Fig. 8(d). The transit time $\hat{T}$ were 90.273, 16.365 and 3.168 under these three velocities, respectively. The flow velocity increased by 5 times, but the observed transit time did not decrease by 5 times. This implies that the transit time is not proportional to the flow velocity.

If a serialized chip was considered, the transit time $\hat{T}$ were 90.273, 88.851 and 78.22 for the cell through three constrictions, respectively, at $v_m = 0.002$ m/s. A significant decrease was observed for these three transit time. This was because the cell preferred a tilted deformation at a low velocity (Kaoui et al., 2009),

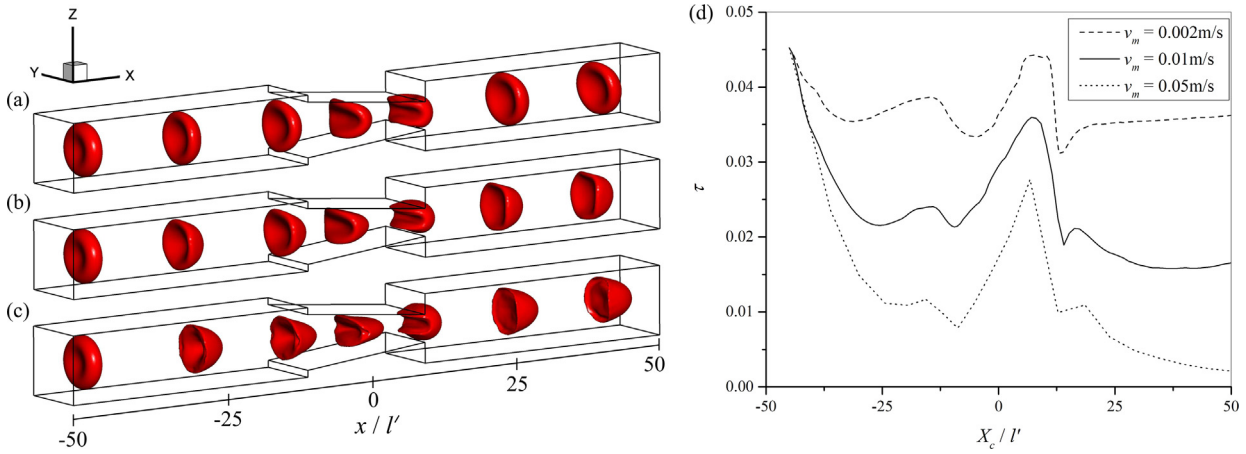

Fig. 8. Motion and deformation of the cell subject to the different mean flow velocities, v_m = 0.002 (a), 0.01 (b) and 0.05 (c) m/s, where the snapshots are taken at similar positions along the microchannel, and the corresponding asphericities (d).

and this tilted deformation had not enough time to recover into a non-tilted shape before encountering the next constriction. At v_m = 0.05 m/s, the transit time $\hat{T}$ were 3.168, 3.19, 3.151, 3.196, 3.231, 3.215, 3.192 and 3.176 for the cell through eight successive constrictions, respectively. These values were quite similar, because the cell preferred a non-tilted deformation at a high velocity (Kaoui et al., 2009). Hence, a flow with a high mean velocity helped in promoting the chip throughput, and also in providing more accurate average transit time of a cell through a serialized chip. At v_m = 0.05 m/s, a cell needs about 2 ms to pass through a unit element (where the hematocrit is about 1%), such that there are about 300,000 cells analyzed in 10 min.

3.5. Heterogeneous multiple cells

Bow et al. (2011) suggested that the microfluidic devices, such as those considered here (Fig. 1), are especially suitable to characterize mechanical properties of heterogeneous cells. In this section, we considered multiple cells with mixed healthy and unhealthy cells. Both the healthy and unhealthy cells had the same geometrical and physical properties, except for their shear moduli. The shear modulus was 6.0×10^{-6} N/m for the healthy cell, but 3.5×10^{-5} N/m for the unhealthy one. The former value may represent a healthy RBC, while the latter one may represent a malaria-infected RBC (Ye et al., 2013). We considered five cases with 2, 3, 5, 8 and 10 cells, respectively. Each case included two simulations; one has no unhealthy cells, and the other has only one unhealthy cell. Then, we compared the transit time between two simulations in each case, for examining the ability of the device in identifying heterogeneous cells.

Fig. 9 shows the motion and deformation of homogeneous and heterogeneous cells through a constriction, from which the following remarks can be drawn: (i) The motion and deformation between the homogeneous and heterogeneous cells were quite similar. This was also found from the two-dimensional cross-sectional shape of deformed cells, as shown in Fig. S3 in the Supplementary Material. Moreover, the average asphericities were quite similar between the homogeneous and heterogeneous cells,

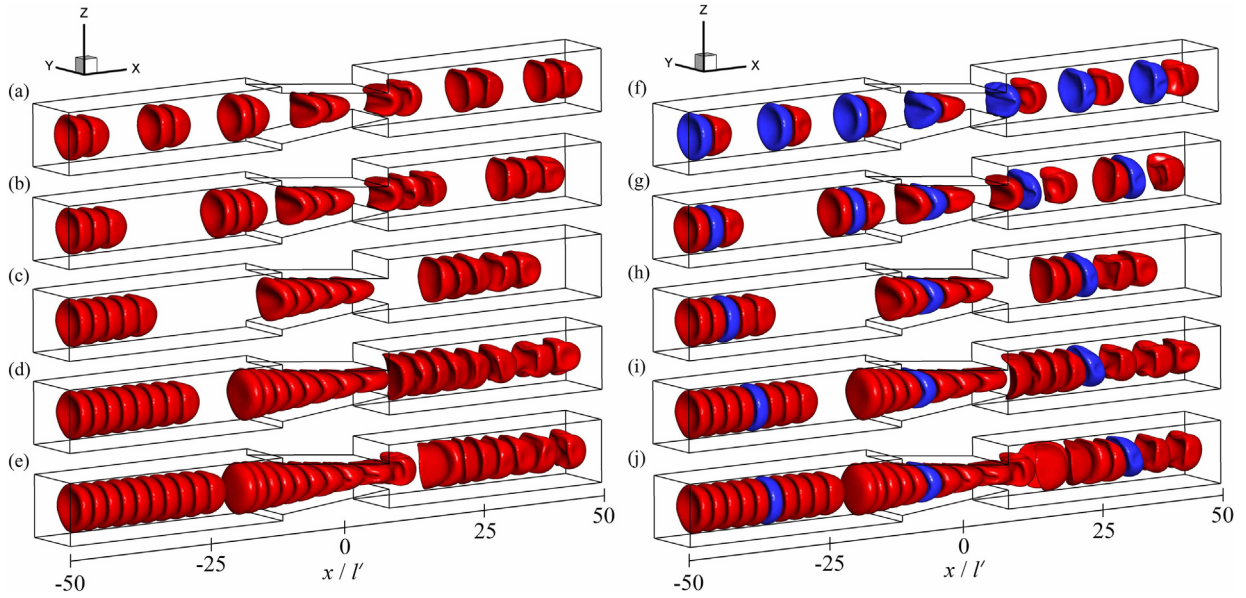

Fig. 9. Motion and deformation of homogeneous (a–e) and heterogeneous (f–j) cells: 2 (a and f), 3 (b and g), 5 (c and h), 8 (d and i) and 10 (e and f), where the cell in red represents the healthy cell, and in blue represents the unhealthy one.

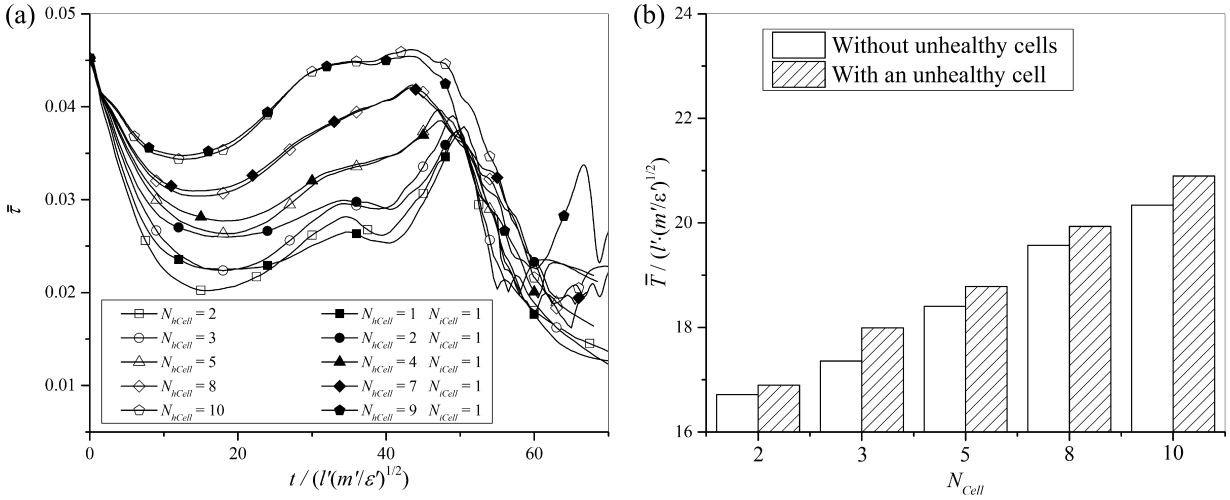

Fig. 10. Average asphericities (a) and average transit time (b) of the homogeneous and heterogeneous cells, where N_{hCell} and N_{iCell} refer to the number of healthy and unhealthy cells, respectively.

as shown in Fig. 10(a). (ii) The cell deformation decreased as the cell number was increased, whether the cells were homogeneous or heterogeneous. This was also obtained from the average asphericities of the cells in Fig. 10(a), where the variation of the average asphericity decreased with increasing cell number, for both the homogeneous and heterogeneous cases. The reason for this was basically that the flow mean velocity decreased as the cell number increased. (iii) The trailing cell became difficult to be folded inward with increasing the cell number, before entering the constriction. Especially for $N_{Cell} = 10$, the trailing cell was even folded outward, as shown in Fig. 9 (e) and (j). This was attributed to the intercellular interaction. As the cell number was increased, the cells moved through the constriction slowly; the intercellular distance became small enough, so that a repulsion happened on two neighbouring cells, causing the trailing cell to be folded outward.

The transit time was different between the homogeneous and heterogeneous cells, although their deformation was found to be similar, as shown in Fig. 10(b). There were two remarkable phenomena observed: (i) that the average transit time increased with increasing the cell number. This was because the flow velocity decreased as the cell number increased. (ii) The transit time for the heterogeneous cells with only one unhealthy cell was larger than that for the homogeneous cells, at a constant cell number. This showed the ability of the designed microchip in characterizing the mechanical properties of heterogeneous cells, even when only one unhealthy cell is included.

4. Conclusions

We investigated numerically a microfluidic chip based on our previous work (Ye et al., 2018b) in its ability to measure cell's mechanical properties of cells, and further examined its performance. We adopted a particle-based numerical method, smoothed dissipative particle dynamics (SDPD), to model the fluid flow, and an immersed boundary method (IBM) to handle the fluid-cell interactions. This combination between SDPD and IBM allowed cells in complex microchannels to be analyzed (Ye et al., 2017b). Two validation studies were then carried out, showing reasonable agreements between our results and the previously-published results (Li et al., 2007; Xiao et al., 2014; Polwaththe-Gallage et al., 2016b). Besides, we pointed out that the numerical model proposed in this work cannot be applicable to nucleated cells, because the interaction is not taken into account between the membrane and nucleus of a cell.

The dependence of the transit time on the cell's shear and bending moduli were tested. If one of mechanical properties (shear or bending modulus) was known, the other can be inferred from the transit time. In order to promote the chip sensitivity, we then carried out a serialization of the chip by periodically arranging a single constriction along the flow direction. The results showed that this operation greatly increased the chip sensitivity. We then studied the effect of the flow velocity on the transit time. The flow with a higher velocity helped to promote the chip throughput, and also to provide more accurate transit time, because a cell preferred a symmetric deformation under a high velocity. Finally, we examined the chip ability on identifying the heterogeneous cells with different mechanical properties, and the results showed that the designed microfluidic chip was indeed capable of identifying heterogeneous cells, even when only one unhealthy cell is included.

5. Conflict of interest

The authors have no conflict of interest.

Acknowledgements

The authors gratefully acknowledge the financial support from the National Natural Science Foundation of China under Project No. 11502094, and from the Special Fund of Industrial Innovation in Jilin Province under Project No. 2016C053-2.

Appendix A. Supplementary material

Supplementary data associated with this article can be found, in the online version, at https://doi.org/10.1016/j.jbiomech.2018.12.019.

References

Bagchi, P., Johnson, P.C., Popel, A.S., 2005. Computational fluid dynamic simulation of aggregation of deformable cells in a shear flow. J. Biomech. Eng. 127, 1070–1080.

Bhattacharjee, S., Elimelech, M., Borkovec, M., 1998. Dlvo interaction between colloidal particles: beyond Derjaguin's approximation. Croat. Chem. Acta 71, 883–903.

Bian, X., Litvinov, S., Qian, R., Ellero, M., Adams, N.A., 2012. Multiscale modeling of particle in suspension with smoothed dissipative particle dynamics. Phys. Fluids 24, 012002.

Bow, H., Pivkin, I.V., Diez-Silva, M., Goldfless, S.J., Dao, M., Niles, J.C., Suresh, S., Han, J.Y., 2011. A microfabricated deformability-based flow cytometer with application to malaria. Lab Chip 11, 1065–1073.
Casquero, H., Bona-Casas, C., Gomez, H., 2017. Nurbs-based numerical proxies for red blood cells and circulating tumor cells in microscale blood flow. Comput. Methods Appl. Mech. Eng. 316, 646–667.
Chien, S., Jan, K., 1973. Ultrastructural basis of the mechanism of rouleaux formation. Microvas. Res. 5, 155–166.
Chung, B., Johnson, P.C., Popel, A.S., 2007. Application of chimera grid to modelling cell motion and aggregation in a narrow tube. Int. J. Numer. Methods Fluids 53, 105–128.
Darling, E.M., Zauscher, S., Block, J.A., Guilak, F., 2007. A thin-layer model for viscoelastic, stress-relaxation testing of cells using atomic force microscopy: do cell properties reflect metastatic potential? Biophys. J. 92, 1784–1791.
Español, P., Revenga, M., 2003. Smoothed dissipative particle dynamics. Phys, Rev. E 67, 026705.
Fedosov, D.A., Caswell, B., Karniadakis, G.E., 2010a. A multiscale red blood cell model with accurate mechanics, rheology, and dynamics. Biophys. J. 98, 2215–2225.
Fedosov, D.A., Caswell, B., Karniadakis, G.E., 2010b. Systematic coarse-graining of spectrin-level red blood cell models. Comput. Meth. Appl. Mech. Eng. 199, 1937–1948.
Fedosov, D.A., Lei, H., Caswell, B., Suresh, S., Karniadakis, G.E., 2011. Multiscale modeling of red blood cell mechanics and blood flow in malaria. PLoS Comput. Biol. 7, e1002270.
Fedosov, D.A., Noguchi, H., Gompper, G., 2014. Multiscale modeling of blood flow: from single cells to blood rheology. Biomech. Model. Mechanobiol. 13, 239–258.
Gambhire, P., Atwell, S., Iss, C., Bedu, F., Ozerov, I., Badens, C., Helfer, E., Viallat, A., Charrier, A., 2017. High aspect ratio sub-micrometer channels using wet etching: application to the dynamics of red blood cell transiting through biomimetic splenic slits. Small 13, 1700967.
Gompper, G., Fedosov, D.A., 2016. Modeling microcirculatory blood flow: current state and future perspectives. Wiley Interdiscip. Rev. Syst. Biol. Med. 8, 157–168.
Groot, R.D., Warren, P.B., 1997. Dissipative particle dynamics: bridging the gap between atomistic and mesoscopic simulation. J. Chem. Phys. 107, 4423–4435.
Guo, Q., Duffy, S.P., Matthews, K., Santoso, A.T., Scott, M.D., Ma, H., 2014. Microfluidic analysis of red blood cell deformability. J. Biomech. 47, 1767–1776.
Guo, Q., Reiling, S.J., Rohrbach, P., Ma, H., 2012. Microfluidic biomechanical assay for red blood cells parasitized by plasmodium falciparum. Lab Chip 12, 1143.
Hosseini, S.M., Feng, J.J., 2009. A particle-based model for the transport of erythrocytes in capillaries. Chem. Eng. Sci. 64, 4488–4497.
Hosseini, S.M., Feng, J.J., 2012. How malaria parasites reduce the deformability of infected red blood cells. Biophys. J. 103, 1–10.
Hou, H.W., Li, Q.S., Lee, G.Y.H., Kumar, A.P., Ong, C.N., Lim, C.T., 2009. Deformability study of breast cancer cells using microfluidics. Biomed. Microdevices 11, 557–564.
Huang, Z., Li, X., Martins-Green, M., Liu, Y., 2012. Microfabrication of cylindrical microfluidic channel networks for microvascular research. Biomed. Microdevices 14, 873–883.
Imai, Y., Omori, T., Shimogonya, Y., Yamaguchi, T., Ishikawa, T., 2016. Numerical methods for simulating blood flow at macro, micro, and multi scales. J. Biomech. 49, 2221–2228.
Kaoui, B., Biros, G., Misbah, C., 2009. Why do red blood cells have asymmetric shapes even in a symmetric flow? Phys. Rev. Lett. 103, 188101.
Koohyar, V., Peter, B., Prosenjit, B., 2016. Flow of red blood cells in stenosed microvessels:. Sci. Rep. 6, 28194.
Li, J., Dao, M., Lim, C.T., Suresh, S., 2005. Spectrin-level modeling of the cytoskeleton and optical tweezers stretching of the erythrocyte. Biophys. J. 88, 3707–3719.
Li, J., Lykotrafitis, G., Ming, D., Suresh, S., 2007. Cytoskeletal dynamics of human erythrocyte. Proc. Nat. Acad. Sci. 104, 4937–4942.
Litvinov, S., Ellero, M., Hu, X., Adams, N.A., 2009. Self-diffusion coefficient in smoothed dissipative particle dynamics. J. Chem. Phys. 130, 021101.
Litvinov, S., Ellero, M., Hu, X.Y., Adams, N.A., 2010. A splitting scheme for highly dissipative smoothed particle dynamics. J. Comp. Phys. 229, 5457–5464.
Liu, Y.L., Liu, W.K., 2006. Rheology of red blood cell aggregation by computer simulation. J. Comput. Phys. 220, 139–154.
Moon, J.Y., Tanner, R.I., Lee, J.S., 2016. A numerical study on the elastic modulus of volume and area dilation for a deformable cell in a microchannel. Biomicrofluidics 10, 044110.
Nematbakhsh, Y., Lim, C.T., 2015. Cell biomechanics and its applications in human disease diagnosis. Acta Mech. Sin. 31, 268–273.
Neu, B., Meiselman, H.J., 2002. Depletion-mediated red blood cell aggregation in polymer solutions. Biophys. J. 83, 2482–2490.
Noguchi, H., Gompper, G., 2005. Vesicle dynamics in shear and capillary flows. J. Phys. 17, S3439–S3444.
Peskin, C.S., 2002. The immersed boundary method. Acta Numer. 11, 1–39.
Pivkin, I.V., Caswell, B., Karniadakis, G.E., 2011. Dissipative particle dynamics. Rev. Comput. Chem. 27, 85–110.
Pivkin, I.V., Karniadakis, G.E., 2008. Accurate coarse-grained modeling of red blood cells. Phys. Rev. Lett. 101, 118105.
Pivkin, I.V., Peng, Z.L., Karniadakis, G.E., Buffet, P.A., Dao, M., Suresh, S., 2016. Biomechanics of red blood cells in human spleen and consequences for physiology and disease. Proc. Natl. Acad. Sci. 113, 7804–7809.
Polwaththe-Gallage, H.N., Saha, S.C., Sauret, E., Flower, R., Gu, Y., 2016a. A coupled sph-dem approach to model the interactions between multiple red blood cells in motion in capillaries. Int. J. Mech. Mater. Des., 1–18
Polwaththe-Gallage, H.N., Saha, S.C., Sauret, E., Flower, R., Gu, Y., 2016b. Sph-dem approach to numerically simulate the deformation of three-dimensional rbcs in non-uniform capillaries. Biomed. Eng. Online 15, 161.
Serrano-Alcalde, F., Garcia-Aznar, J.M., Gomez-Benito, M.J., 2017. The role of nuclear mechanics in cell deformation under creeping flows. J. Theo. Biol. 432, 25–32.
Shelby, J.P., White, J., Ganesan, K., Rathod, P.K., Chiu, D.T., 2003. A microfluidic model for single-cell capillary obstruction by plasmodium falciparum-infected erythrocytes. Proc. Natl. Acad. Sci. 100, 14618–14622.
Shirai, A., Fujita, R., Hayase, T., 2003. Transit characteristics of a neutrophil passing through a circular constriction in a cylindrical capillary vessel. JSME Int. J. 46, 1198–1207.
Skalak, R., Tozeren, A., Zarda, R.P., Chien, S., 1973. Strain energy function of red blood cell membrane. Biophys. J. 13, 245–264.
Skalak, R., Zarda, P.R., Jan, K.M., Chien, S., 1981. Mechanics of rouleau formation. Biophys. J. 35, 771–781.
Suresh, S., 2006. Mechanical response of human red blood cells in health and disease: some structure-property-function relationships. J. Mater. Res. 21, 1871–1877.
Suresh, S., Spatz, J., Mills, J.P., Micoulet, A., Dao, M., Lim, C.T., Beil, M., Seufferlein, T., 2005. Connections between single-cell biomechanics and human disease states: gastrointestinal cancer and malaria. Acta Biomater. 1, 15–30.
Suresh, S., Spatz, J., Mills, J.P., Micoulet, A., Dao, M., Lim, C.T., Beil, M., Seufferlein, T., 2015. Reprint of: connections between single-cell biomechanics and human disease states: gastrointestinal cancer and malaria. Acta Biomater. 23, 3–15.
Tian, T., Zhai, Q., Zhang, R., 2018. A new modified weak Galerkin finite element scheme for solving the stationary stokes equations. J. Comput. Appl. Math.
Whitesides, G.M., 2006. The origins and the future of microfluidics. Nature 442, 368.
Xiao, L.L., Chen, S., Lin, C.S., Liu, Y., 2014. Simulation of a single red blood cell flowing through a microvessel stenosis using dissipative particle dynamics. Mol. Cell. Biomech. 11, 67–85.
Xiao, L.L., Liu, Y., Chen, S., Fu, B.M., 2016. Simulation of deformation and aggregation of two red blood cells in a stenosed microvessel by dissipative particle dynamics. Cell Biochem. Biophys. 74, 513–525.
Xu, W.W., Mezencev, R., Kim, B., Wang, L.J., McDonald, J., Sulchek, T., 2012. Cell stiffness is a biomarker of the metastatic potential of ovarian cancer cells. Plos One 7, e46609.
Ye, T., Peng, L., Li, Y., 2018a. Three-dimensional motion and deformation of a red blood cell in bifurcated microvessels. J. Appl. Phys. 123, 064701.
Ye, T., Phan-Thien, N., Khoo, B.C., Lim, C.T., 2013. Stretching and relaxation of malaria-infected red blood cells. Biophys. J. 105, 1103–1109.
Ye, T., Phan-Thien, N., Khoo, B.C., Lim, C.T., 2014. A file of red blood cells in tube flow: a three-dimensional numerical study. J. Appl. Phys. 116, 562–568.
Ye, T., Phan-Thien, N., Lim, C.T., 2016. Particle-based simulations of red blood cells-a review. J. Biomech. 49, 2255–2266.
Ye, T., Phan-Thien, N., Lim, C.T., Li, Y., 2017a. Red blood cell motion and deformation in a curved microvessel. J. Biomech. 65, 12–22.
Ye, T., Phan-Thien, N., Lim, C.T., Peng, L.N., Shi, H.X., 2017b. Hybrid smoothed dissipative particle dynamics and immersed boundary method for simulation of red blood cells in flows. Phys. Rev. E 95, 063314.
Ye, T., Shi, H., PhanThien, N., Lim, C., Li, Y., 2018b. Relationship between transit time and mechanical properties of a cell through a stenosed microchannel. Soft Matter 14, 533–545.
Ye, T., Shi, H.X., Peng, L.N., Li, Y., 2017c. Numerical studies of a red blood cell in rectangular microchannels. J. Appl. Phys. 122, 084701.
Zhang, H., Liu, J., Cao, Y., Wang, Y., 2013. Effects of particle size on lignite reverse flotation kinetics in the presence of sodium chloride. Powder Tech. 246, 658–663.
Zhang, J., Johnson, P.C., Popel, A.S., 2008. Red blood cell aggregation and dissociation in shear flows simulated by lattice boltzmann method. J. Biomech. 41, 47–55.
Zhang, J., Johnson, P.C., Popel, A.S., 2009. Effects of erythrocyte deformability and aggregation on the cell free layer and apparent viscosity of microscopic blood flows. Microvas. Res. 77, 265–272.